Numerical modeling of TeraHertz electronic devices

**L. Varani · C. Palermo · J. F. Millithaler ·
J. C. Vaissière · E. Starikov · P. Shiktorov ·
V. Gružinskis · J. Mateos · S. Pérez · D. Pardo ·
T. González**

Abstract We investigate by means of Monte Carlo simulations the physical processes associated with the emission of TeraHertz radiation in different electronic devices. We analyze four alternative and complementary strategies which seem to be promising candidates to obtain the TeraHertz emission: (1) a nitride maser based on the optical-phonon transit-time resonance, (2) the high–order harmonic generation in bulk materials and nanometric Schottky-barrier diodes, (3) the excitation of coherent plasma oscillations in micron and submicron diodes, (4) the current instabilities and plasma oscillations in high electron mobility transistors (HEMT). The numerical results show that several physical mechanisms can be exploited to increase significantly the operating frequency of these devices and the best conditions to optimize the radiation emission in the TeraHertz range are studied in detail.

Keywords TeraHertz · Monte Carlo · Nitrides · Plasma oscillations

L. Varani (✉) · C. Palermo · J. F. Millithaler · J. C. Vaissière
Centre d'Electronique et de Micro–optoélectronique de
Montpellier (CNRS–UMR 5507), Université Montpellier II,
place E. Bataillon, 34095 Montpellier, France
e-mail: varani@cem2.univ-montp2.fr

E. Starikov · P. Shiktorov · V. Gružinskis
Semiconductor Physics Institute, A. Goštauto 11, 2600 Vilnius,
Lithuania

J. Mateos · S. Pérez · D. Pardo · T. González
Universidad de Salamanca, Dpt. de Física Aplicada, Plaza de la
Merced s/n, 37008 Salamanca, Spain

1. Introduction

The part of the electromagnetic spectrum between millimeter waves and far infrared is referred to as TeraHertz (THz) radiation or T–rays [1]. Much of the recent interest in THz radiation stems from its ability to penetrate deep into many organic materials without the damage associated with ionizing radiation such as X-rays. Additionally, since THz radiation is readily absorbed by water, it can be used to distinguish between materials with varying water content. These properties can lead to very appealing applications in biomedical imaging [2]. THz radiation can also penetrate poor weather, dust and smoke far better than infrared or visible systems. For this reason defence and security applications are also envisaged. Furthermore the ability to penetrate dielectrics such as windows, paper, clothing and in certain instances even walls, has opened up the opportunity to reveal concealed explosives, metallic and non-metallic weapons (such as ceramic, plastic or composite guns and knives), chemical weapons and other threats hidden in packages. THz detection is also a very interesting field for astronomers: much of the photons generated in the Big Bang fall into the submillimeter and far-infrared region of the spectrum. Nondestructive testing of integrated circuits is also a future area of application [3].

However, it is difficult to reach the THz range using electronic or optical approaches. At present, there exist few methods of generating THz radiation from solids: some of them are based on plasma excitations by femtosecond laser pulses in low dimensional [4] and bulk [5] semiconductors or superconductors [6], while other ones rely on mixing of laser beams with close frequencies [4]. These methods require advanced experimental equipments and their performances depend on a strong optical excitation of an appropriate semiconductor structure. On the other hand, THz radiation can

also be generated by p–Ge [7, 8] and quantum cascade [9] lasers.

Probably the most interesting devices, from the application point of view, seems to be THz sources based on solid state devices, since they offer better possibilities of integration with other optoelectronic devices within a single chip. Therefore, in this article, we study by numerical simulation four different strategies to obtain the emission of THz radiation from electronic devices. The first one (treated in Section 2) is based on the amplification of electromagnetic radiation inside a MASER whose active medium is made up of a nitride layer; the second one relies on the generation of high-order harmonics in bulk materials and nanometric Schottky barrier diodes under cyclostationary large-signal conditions (see Section 3); the third one (presented in Section 4) is based on the excitation of coherent plasma oscillations in submicron diodes and finally the fourth one exploits different current and plasma instabilities in high electron mobility transistors (see Section 5).

2. Maser

It is well known that nitrides are promising candidates for high-power, high-temperature microwave and optoelectonic devices [10, 11]. Here we want to show that, due to the high value of the optical-phonon energy and the strong interaction of carriers with optical phonons, nitrides (and in particular GaN) can be also considered as promising materials for low-temperature THz generators based on the dynamical peculiarities of quasiballistic motion of carriers inside the optical phonon sphere of momentum space. In this case the generation is associated with the periodic motion of carriers inside the optical phonon sphere of momentum space when a constant electric field E_0 is applied to a bulk GaN. Because of the acceleration from the electric field, the carrier moving quasiballistically up to the optical phonon energy $\hbar\omega_0$, will suddenly emit an optical phonon and instantaneously return

inside the optical phonon sphere, where the carrier then starts the next cycle of acceleration. The characteristic time of such a cyclic process is inversely proportional to the applied electric field and given by $\tau_E = p_0/(eE_0)$, where p_0 is the optical-phonon momentum. The weaker the intensity of carrier scattering inside the optical phonon sphere and the penetration of carriers outside the sphere is, the higher the coherence of successive free flights of a single carrier will be. These conditions are usually fulfilled at low lattice temperatures in materials with a steep increase of the polar optical phonon emission intensity. In standard III–V semiconductors, such as GaAs and InP, the maximum generation frequency was predicted to be in the range of 300–400 GHz [12, 13]. By contrast, with the wide-gap materials, such as GaN, one can expect a considerable increase in the maximum generation frequency and a general improvement of the conditions for dynamic negative differential mobility (DNDM), as a consequence of a higher value of $\hbar\omega_0$, and a stronger interaction of electrons with optical phonons [14, 15].

Using the Monte Carlo (MC) algorithm described in detail in Ref. [14] we have calculated the frequency dependence of the complex differential mobility: here the optical phonon resonance has been found to manifest itself as a sequence of minima corresponding to the first and higher harmonics of the resonant frequency $\nu_E = 1/\tau_E$. As follows from Fig. 1(a), the generation frequency can be easily tuned by means of the static electric field magnitude. The total amplification band is rather wide and, at $T = 10$ K, it covers practically the whole submillimeter region starting at $f = 0.2$ THz ($\lambda = 1.5$ mm) and ending at $f = 3$ THz ($\lambda = 0.1$ mm). For a given value of E_0 the amplification band is very narrow (see curves 3 and 4), and the optimum amplification frequency, corresponding to the maximum value of the DNDM in the band, increases practically linearly with E_0 in full agreement with the simple relation $\nu_E = 1/\tau_E = eE_0/p_0$. With the increase of the temperature, both the narrow character of the amplification band at a fixed E_0 and the linear increase of the optimum frequency of amplification remain the same. However, the
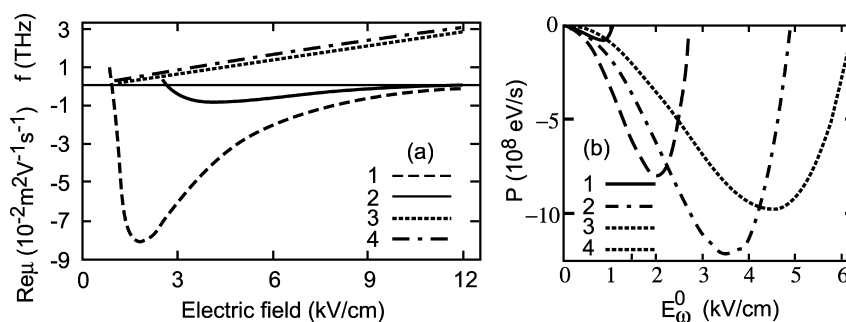
Fig. 1 Maximum value of the DNDM (curve 1) and lower and upper frequency limits of the amplification band (curves 3 and 4, respectively) calculated for wurtzite GaN as a function of the electric field E_0 at $T_0 = 10$ K, with $N_d = 10^{16}$ cm^{-3}. Curve 2 refers to the maximum value of the DNDM at $T_0 = 80$ K for $N_d = 10^{16}$ cm^{-3} (a). Power generated at

the fundamental frequencies of $f = 0.25, 0.5, 1$, and 1.5 THz (curves 1 to 4 with, respectively, the static electric fields of $E_0 = 1.2, 2.25, 4.3$, and 6.35 kV/cm) as a function of the amplitude of the microwave field calculated in wurtzite GaN with a doping level of $N_d = 10^{16}$ cm^{-3} at $T_0 = 10$ K (b)

total frequency range of possible amplification narrows down because the electric field range corresponding to streaming conditions also narrows down with the increase of scattering intensity inside the optical phonon sphere. Moreover, the maximum values of the DNDM decreases with the increase of the temperature even if the amplification in the THz frequency range persists at liquid nitrogen temperatures. This persistence is very important for a technological application of the effect since liquid nitrogen temperatures are preferable for practical use.

To achieve actual power generation it is necessary to put the active medium into a resonator system to obtain enough output power. To calculate the generated power P_ω it is sufficient to introduce the microwave electric field of the amplified mode $E_{m\omega}(t) = \Re[E_\omega \exp(i\omega t)]$ directly into the equation of motion $\dot{p}_x(t) = eE_0 + eE_\omega \cos(\omega t)$, which describes the free flight of a trial particle in momentum space (see Refs. [14,15] for the details of the numerical procedure). Figure 1(b) summarizes the results of the field dependence of the power generated at frequencies of $f = 0.25, 0.5, 1$, and 1.5 THz with, respectively, the static electric fields of $E_0 = 1.2, 2.25, 4.3$, and 6.35 kV/cm. Each field corresponds to the maximum value of the negative differential mobility at the given frequency. At low field amplitudes, the generated power increases first as $|E_\omega^0|^2$, then reaches the maximum values when $E_\omega^0 = 0.7 - 0.9\,E_0$ and finally decreases to zero when E_ω reaches 1–1.2 E_0 at each given frequency. In the presence of DNDM, an external resonant system leads to the onset and increase in microwave oscillations accompanied by an increase in the amplitude of the microwave field E_ω inside the sample. At the initial stage these increases are accompanied by the increase in the microwave power P_ω which, under small-signal conditions, is proportional to $\Re[\mu_\omega E_\omega^2]$. However, a considerable increase in E_ω results in a decrease of the differential mobility and of the dynamical gain. Finally, when both the gain and the generated power go down to zero, the amplification effect disappears completely.

3. Harmonic generation

Due to their strongly nonlinear current-voltage (I-V) and capacitance-voltage (C-V) characteristics, GaAs Schottky-barrier diodes (SBDs) are widely used in modern solid-state electronics as frequency multipliers in the subterahertz region [16–18] and mixers in the superterahertz region [18–20]. As a consequence, the intensity of fundamental and higher order harmonics of the current response, the intrinsic noise, and the signal-to-noise ratio of these devices are relevant parameters when assessing their electrical performances under high-frequency large-signal operation. For this sake, we consider the room temperature operation of a heavily doped GaAs $n^+ - n-$metal SBD with n region length $l_n = 0.03\ \mu$m, barrier height $U_b = 1.03$ V, carrier concentrations $n^+ = 8 \times 10^{18}$ cm^{-3} and $n = 1.1 \times 10^{18}$ cm^{-3}. The kinetic equation coupled with the Poisson equation for the self-consistent electric field is solved by the MC method [21,22]. A $\Gamma - L - X$ nonparabolic spherically symmetric conduction band model and all main scattering mechanisms are accounted for in the MC simulations in accordance with [23]. The degeneracy effect is included by determining the final state after scattering with the rejection procedure of [24]. We are interested in large-signal operation near flat–band conditions, where Schottky diodes typically work. In this regime tunneling current plays a negligible role as compared to thermionic and displacement currents, and thus it is omitted. The details of the numerical procedure can be found in Refs. [25–27].

Figure 2(a) reports the instantaneous total current density, $\langle j(t) \rangle$, flowing through the SBD as a function of the instantaneous values of the applied voltage $U(t) = U_0 + U_1 \sin(2\pi ft)$ during a period of $U(t)$ oscillations for frequencies $f = 0.05, 0.5, 2$ THz (curves 1 to 3, respectively). Here brackets $\langle \ldots \rangle$ denote averaging over a large number of successive periods simulated by MC calculations. The values $U_0 = 0.7$ V and $U_1 = 0.3$ V are taken to exploit in the most effective way the nonlinear region of the I-V and C-V
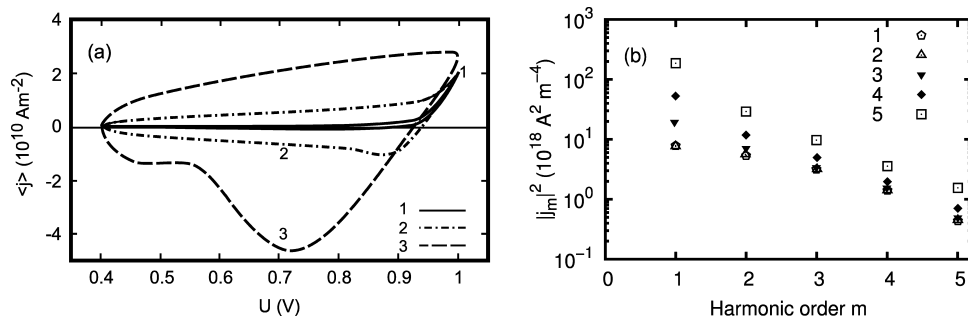
Fig. 2 Instantaneous total current density $\langle j \rangle$ as a function of the instantaneous periodic voltage $U(t) = U_0 + U_1 \sin(2\pi ft)$ applied to the SBD, with $U_0 = 0.7$ V, $U_0 = 0.3$ V and frequencies $f = 0.05, 0.5, 2$ THz (curves 1 to 3, respectively) (a). Square amplitudes of the first five harmonics of the total current density as functions of the harmonic order number m calculated for the same conditions at frequencies $f = 0.05, 0.1, 0.5, 1$, and 2 THz (symbols 1 to 5, respectively) (b)

characteristics associated with the transition from barrier-limited to flat-band conditions. This region corresponds to applied voltages comparable with the barrier height U_b . As follows from Fig. 2(a), the inertia of the current response is absent up to $f \simeq 0.1$ THz. Here the $\langle j(U) \rangle$ diagram follows practically the static I-V relation. At $f > 0.1$ THz, the instantaneous $\langle j(U) \rangle$ characteristic begins to differ significantly from that of the static case. The hysteresis-like behavior of $\langle j(U) \rangle$ is accompanied by a rapid increase with f of the amplitude of both the fundamental and the higher order harmonics, which is typical for the strong C-V nonlinearity of varactors [18]. This is illustrated by Fig. 2(b), which shows the squared amplitudes of the first five generated harmonics. For the SBD under test, the C-V nonlinearity dominates over the I-V nonlinearity in the frequency range 0.2–5 THz. With a further increase of f , the C-V nonlinearity becomes ineffective, since when approaching the returning carrier resonance [21] the displacement of the depletion region boundary no longer follows the instantaneous value of the applied voltage $U(t)$.

4. Plasma diodes

A promising high-frequency generation mechanism in $n^+ - n - n^+$ semiconductor structures was proposed by Ryzhij et al. [28] about twenty years ago. The mechanism is based on the excitation of coherent electron plasma oscillations by optical phonon emission under near ballistic electron motion in the n-region of the structure [28–31].

To explain qualitatively the appearance of the oscillations let us define the region inside the active region of the diode where the electrons injected from the emitter lose the energy due to optical phonon emissions as the stop place which subdivides the n-region into two parts. These two regions, namely, the region from the emitter up to the stop place and the region between the stop place and the collector cannot conduct the same current. This leads to a space charge accumulation in the n-region and as a consequence to the reduction of electrons injection from the emitter [28]. After the extraction of the excess charge into the collector the

process is repeated. The frequency of current oscillations is the reciprocal of the electron flight time through the structure [29]. In full analogy with the case of bulk materials (see, e.g. [32, 33]), to decrease this time in order to achieve higher frequency of generation it is necessary to increase the average electric field inside the structure. However, in so doing carriers will penetrate more into the energy region above the optical phonon energy $\hbar\omega_0$, so that the simultaneous emission of optical phonons by simultaneously injected carriers loses coherence in time and space. Therefore, the materials with high optical phonon emission rates, which prevent the carrier penetration outside the optical phonon sphere, are preferable for THz frequency generation. The nitride semiconductors ideally fit this requirement.

In order to detect and analyse the onset of high-frequency instabilities, we calculate the spectral densities of current fluctuations inside the structure. When the applied voltage approaches the threshold for an exponential evolution of an instability, a sharp enhancement of the noise takes place in the frequency region characteristic of the instability. Above this threshold, the noise can transform into an harmonic or quasi–harmonic signal, i.e. the generation process originated by the instability starts working. We stress that the upper frequency limit of the various instabilities associated with the plasma oscillations of free carriers in the n region is restricted by a hybrid plasma resonance originated by the $n^+ - n$−homojunction (see, e.g. [34] and references therein). Thus, the appearance of a resonant–like enhancement of the noise at frequencies below that of the $n^+ - n$ hybrid plasma resonance should be considered as an indicator of the onset of an instability which can transform into generation. The effect is more pronounced when the frequency associated with the transit–time through the n-region is close to the plasma frequency of the n-region. This property is a signature to identify the instability (see, e.g., [35, 36] and references therein).

The transition from the stable state of the $n^+ - n - n^+$ structure to the oscillator state due to the instability onset is illustrated in Fig. 3(a). Here, we report the frequency behavior of the current noise and the time behavior of the current flowing through the structure calculated by MC simulations

Fig. 3 (a) Spectral density of current fluctuations at different temperatures T and (b) time dependence of the current at $T = 10$ and 80 K (upper and lower cases, respectively) for a $0.02 - 0.4 - 0.02$ μm n^+nn^+ InN diode $n^+ = 2 \times 10^{18}$ cm^{-3}, $n = 4 \times 10^{16}$ cm^{-3} at a constant applied voltage equal to 0.15 V
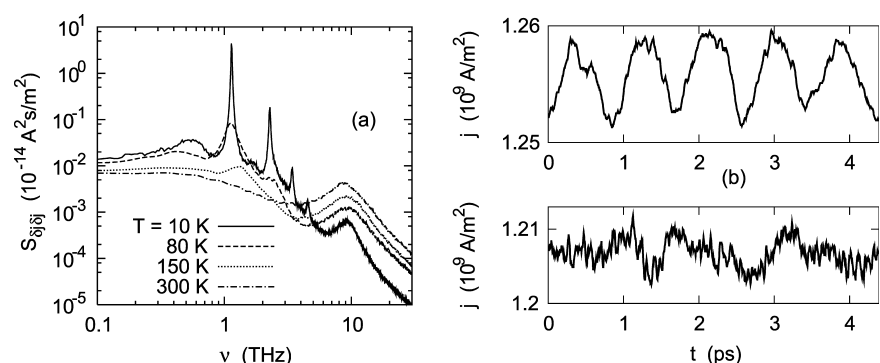
of the electron transport at different lattice temperatures T. At room temperature the spectral density of current fluctuations, $S_{\delta j \delta j}(\nu)$ shows the standard behavior consisting of a low-frequency plateau and a high-frequency peak at 10 THz caused by the hybrid plasma resonance originated by the $n^+ - n-$homojunctions [34]. With the decrease of the temperature, the conditions for a ballistic motion through the n-region are improved. As a consequence, at $T = 80$ K an additional peak of $S_{\delta j \delta j}(\nu)$ at a frequency of 1.14 THz appears. The amplitude of the peak sharply increases at $T = 10$ K. The peak and its harmonics are caused by the streaming plasma instability, as directly evidenced by Fig. 3(b). Indeed, at $T = 10$ K the instantaneous current, $j(t)$, exhibits a near–periodic noisy behavior, while at $T = 80$ K a more random behavior becomes evident. Nevertheless, the current noise spectrum (see Fig. 3(a)) evidences the peak caused by the instability formation already at $T = 80$ K.

5. HEMT

The aim of this Section is to give a more complete description and analysis of the THz emission in nanometric lattice-matched InGaAs/InAlAs HEMT on InP substrate grown by molecular-beam epitaxy recently observed in experiments [37, 38]. Due to the nanometric gate length, very high electric fields appear locally and lead to the presence of hot carrier phenomena and ballistic transport. For the special case of heterostructure devices, the physical scenario becomes particularly complex due to the appearance of quantum effects associated with energy quantization in the transversal dimension within the channel, degeneracy due to the high carrier concentration and tunnelling from the channel into the gate due to the very thin barrier layer. In our simulations degeneracy effects are locally taken into account using the rejection technique [39], while other quantum effects have been neglected in order to have reasonable CPU times. However, being the plasma oscillations a collective motion arising from Coulomb interaction among carriers,

the main features of this phenomenon are taken into account correctly in this semi–classical MC model.

Another interesting mechanism known to be able to produce oscillations in III-V semiconductor devices is the Gunn Effect. Under the effect of a strong electric field the electron effective mass increases as a consequence of intervalley transfer (i.e. negative differential resistance mechanism), thus originating the formation of a Gunn domain, that under certain conditions can produce current oscillations. Up to now, the only way for Gunn-diode based circuits to reach the THz range is by means of frequency multipliers [40]. However, as we will show, numerical results seem to indicate that Gunn oscillations in nanometer–scale devices can reach the THz range. The details of the microscopic model and of the simulated structure can be found in Ref. [38].

Figure 4(a) shows the gate current noise spectra for several values of the drain-to-source voltage and $V_{GS} = 0.05$ V obtained with MC simulations of similar HEMTs (those studied in [41]). There are two maxima on each spectrum: the low frequency (LF) one around 2 THz and the high frequency (HF) one at 5 THz. The position of the HF maximum does not depend on the drain voltage while the LF maximum moves to higher frequencies when the drain voltage increases. This is exactly what is observed in the experimental spectra [38]. Looking at the experimental I–V curves which exhibit kinks in correspondence to the onset of THz emission [38] one may think that the detected emission could take place due to Gunn oscillations since their onset leads to a decrease of the drain current, and this effect has already been experimentally detected in HEMTs [42]. In order to explain the origin of the emission we have performed MC simulations of HEMTs with different geometries and we have observed that, under certain conditions, Gunn oscillations take place when V_{DS} is higher than a given threshold value as shown in Fig. 4(b). The Gunn oscillations appear for frequencies around 1.5 THz, which confirms that this mechanism can be responsible for the LF peaks observed in the measurements. It is also interesting to note that the noise spectra for V_{DS} below the Gunn onset show a peak at frequencies
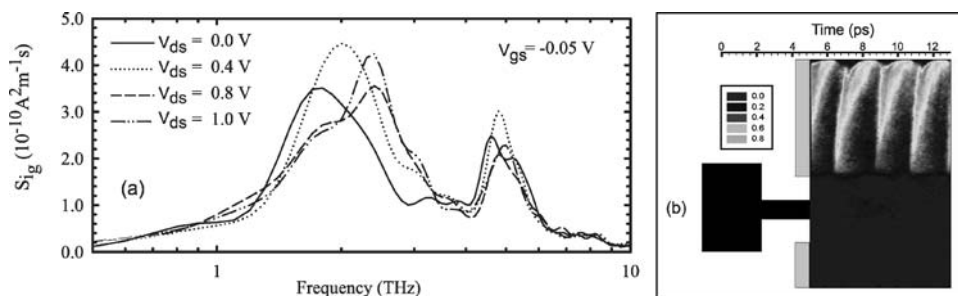
Fig. 4 Gate current noise spectra for the indicated drain-to-source applied voltages at a constant $V_{GS} = -0.05$ V (a). Bidimensional map of the L–valley population in the simulated HEMT. The gray levels represents the fraction of carriers populating the L–valley according to the

reported values (lighter gray corresponds to higher population values). The vertical axis corresponds to the longitudinal transistor direction while the horizontal axis represents the time according to the reported scale (b)

around 1 THz, even if the amplitude of the oscillations is not detectable yet. In contrast, the HF peak of the measured spectrum can only be interpreted as a consequence of plasma oscillations in the device, which are not much dependent on the biasing. This is because the plasma frequency is associated with the concentration of electrons in the whole channel, and this quantity is nearly constant. This agreement is unexpectedly good due to several reasons: different temperature conditions (4.2 K for the emission measurements and 300 K for the noise simulation) and the semiclassic nature of the MC model (at 4.2 K quantum effects in the channel of the HEMT can be very important but they are not considered in the simulation). Therefore, to improve the physical model, the influence of the T-shape of the gate electrode and quantum effects will be the subject of future investigations.

6. Conclusions

We have reported results of Monte Carlo simulations performed for different electronic devices in order to obtain emission of electromagnetic radiation in the TeraHertz range. The main advantages of the studied devices can be summarized as follows:

1. for the nitride maser a high value of the maximum amplification coefficient ($\simeq 100$ cm^{-1}) and a wide tuning range of frequency, covering the whole submillimeter range ($f \simeq 0.3$–3 THz), obtainable by using only an applied electric field;
2. for the case of high-order harmonic generation in nanometric Schottky-barrier diodes, the possibility of room-temperature working operation as well as the possibility to optimize the emitted power by an appropriate choice of the device geometry;
3. for the plasma diodes the possibility to tune the emission frequency by a variable capacitance connected in a parallel resonant circuit and the independence of this frequency of the device length;
4. for the nanometric HEMTs the possibility to use the same kind of device as emitter or detector and the tuning of the emission frequency by changing the voltage applied to gate and drain electrodes.

All these numerical results confirm that several candidates exist to obtain TeraHertz emitters using simple electronic devices which offer promising perspectives for large-scale integration and applications.

References

1. Sensing with THz Radiation. Mittleman D. (eds.), Springer, Berlin (2003)
2. Beard, M.C., Turner, G.M., Schmuttenmaer, C.A.: Phys. Med. Biol. **47**, 3841 (2002)
3. See for example the webpage of Teraview, www.teraview.co.uk, a commercial company that exploits several application of Terahertz light.
4. Sekine, N., Hirakawa, K., Vosseburger, M., Bolivar, P.H., Kurz, H.: Phys. Rev. B **64**, 201323/1–4 (2001)
5. Heyman, J.N., Neocleous, P., Hebert, D., Crowell, P.A., Muller, T., Unterrainer, K.: Phys. Rev. B **64**, 085202/1–7 (2001)
6. Iguchi, I.: Superconductor Science Technology **13**, 93 (2000).
7. Hoffmann, S., Hofmann, M., Brundermann, E., Havenith, M., Matus, M., Moloney, J.V., Moskalenko, A.S., Kira, M. Koch, S.W., Saito, S., Sakai, K.: Appl. Phys. Lett. **84**, 3585 (2004)
8. Andronov, A.A., Kozlov, V.A., Pavlov, S.A., Pavlov, S.G.: Soviet Technical Physics Letters **14**, 891 (1988)
9. Kohler, R. Tredicucci, A., Mauro, C., Beltram, F., Beere, H.E., Linfield, E.H., Davies, A.G., Ritchie, D.A.: Appl. Phys. Lett. **84**, 1266 (2004)
10. Shur, M.S., Gaska, R., Bykhovski, A.: Solid-State Electron. **43**, 1451 (1999)
11. Burk Jr. A.A. et al.: Solid–State Electron **43**, 1459 (1999)
12. Pozhela, Y.K., Starikov, E.V., Shiktorov, P.N.: Semicond. Sci. Technol. **7**, B386 (1992)
13. Starikov, E.V., Shiktorov, P.N.: Lietuvos Fiz. Rinkinis **32**(4), 471 (1992)
14. Starikov, E., Shiktorov, P., Gruzhinskis, V., Reggiani, L., Varani, L., Vaissière, J.C., Zhao, J.H.: J. Appl. Phys. **89**, 1161 (2001)
15. Starikov, E., Shiktorov, P., Gruzhinskis, V., Reggiani, L., Varani, L., Vaissière, J.C., Zhao, J.H.: IEEE Trans. Electr. Dev. **48**, 438 (2001)
16. Rydberg, A., Lyons, B.N., Lidholm, S.U.: IEEE Trans. Microwave Theory Tech. **40**, 827 (1992)
17. Jelenski, A., Grub, A., Krozer, V., Hartnagel, H.L.: IEEE Trans. Microwave Theory Tech. **41**, 549 (1993)
18. Crowe, T.W., Hesler, J.L., Weikle, R.W., Jones, S.H.: Infr. Phys. Technol. **40**, 175 (1999)
19. Crowe, T.W.: Int. J. Infr. Millim. Waves **10**, 765 (1989)
20. Gelmont, B.L., Woolard, D.L., Hesler, J.L., Crowe, T.W.: IEEE Trans. Electron Devices **45**, 2521 (1998)
21. Gonzalez, T., Pardo, D., Reggiani, L., Varani, L.: J. Appl. Phys. **82**, 2349 (1997)
22. Starikov, E., Shiktorov, P., Gružinskis, V., Nougier, J.P. Vaissière, J.C., Varani, L., Reggiani, L.: J. Appl. Phys. **79**, 242 (1996)
23. Brennan K., Hess, K.: Solid–State Electron. **27**, 347 (1984)
24. M. V. Fischetti and S. E. Laux, Phys. Rev. B, **38**, 9721 (1988)
25. Shiktorov, P., Starikov, E., Gruzhinskis, V., Reggiani, L., Varani, L., Vaissière, J.C.: IEEE Trans. Electron Dev. **50**, 1171 (2003)
26. Shiktorov, P., Starikov, E., Gruzhinskis, V., Pérez, S., González, T., Reggiani, L., Varani, L., Vaissière, J.C.: IEEE Electr. Dev. Lett. **25**, 1 (2004)
27. Persano Adorno, D., Zarcone, M., Ferrante, G., Shiktorov, P., Starikov, E., Gružinskis, V., Pérez, S., González, T., Reggiani, L., Varani, L., Vaissière, J.C.: Phys. Stat. Sol. (c) **1**(6), 1367 (2004)

28. Ryzhij, V.I., Bannov, N.A., Fedirko Fiz. Tekh. Poluprovodn, V.A.: V. **8**, 769 (1984)
29. Bannov, N.A., Ryzhij, V.I., Svjatchenko Elektron, A.A.: Tekh., Ser. 3, Mikroelektron. **1**, 22 (1984)
30. Gružinskis, V., Reklaitis, A.: Electron. Lett. **19**, 733 (1983)
31. Bannov, N., Gružinskis, V., Reklaitis, A., Ryzhij, V.: Solid state electron. **29**, 1207 (1986)
32. Starikov, E., Shiktorov, P., Gružinskis, V., Reggiani, L., Varani, L., Vaissière, J.C., Zhao., J.H.: J. Appl. Phys. **89**, 1161 (2001)
33. Starikov, E., Shiktorov, P., Gru°zinskis, V., Reggiani, L., Varani, L., Vaissière, J.C., Zhao., J.H.: J. Phys. Condens. Matter **13**, 7159 (2001)
34. Starikov E. et al.: J. Appl. Phys. **79**, 242 (1996)
35. Bannov N., et al.: Solid State Electron. **29**, 1207 (1986)
36. Starikov E. et al.: Phys. Stat. Sol. (a) **190**, 287 (2002)
37. Knap W. et al.: Appl. Phys. Lett. **84**, 2331 (2004)
38. Lusakowski J. et al.: J. Appl. Phys. **97**, 064307 (2005)
39. Mateos, J., Gonzalez, T., Pardo, D., Hoel, V., Cappy, A.: IEEE Trans. Electron Dev. **47**, 250 (2000)
40. Maestrini, A., Ward, J., Gill, J., Javadi, H., Schlecht, E., Chattopadhyay, G., Maiwald, F., Erickson, N.R., Mehdi, I.: IEEE Microwave and Wireless Components Letters **14**, 253 (2004)
41. Mateos, J., Gonz·lez, T., Pardo, D., Bollaert, S., Parenty, T., Cappy, A.: IEEE Trans. Electron. Dev. **51**, 521 (2004), and IEEE Trans. Electron. Dev. **51**, 1228 (2004)
42. Dunn, G.M., Phillips, A., Topham, P.J.: Semicond. Sci. Technol. **16**, 562 (2001)